The Astrophysical Journal, 925:55 (10pp), 2022 January 20 https://doi.org/10.3847/1538-4357/ac3cb9

Warm Absorbers in the Radiation-driven Fountain Model of Low-mass Active Galactic Nuclei

Shoji Ogawa[1], Yoshihiro Ueda[1], Keiichi Wada[2,3,4], and Misaki Mizumoto[1,5]
[1] Department of Astronomy, Kyoto University, Kitashirakawa-Oiwake-cho, Sakyo-ku, Kyoto 606-8502, Japan; ogawa@kusastro.kyoto-u.ac.jp
[2] Kagoshima University, Graduate School of Science and Engineering, Kagoshima 890-0065, Japan
[3] Ehime University, Research Center for Space and Cosmic Evolution, Matsuyama 790-8577, Japan
[4] Hokkaido University, Faculty of Science, Sapporo 060-0810, Japan
[5] Hakubi Center, Kyoto University, Yoshida-honmachi, Sakyo-ku, Kyoto, 606-8501, Japan
Received 2021 October 19; revised 2021 November 14; accepted 2021 November 22; published 2022 January 25

Abstract

To investigate the origins of the warm absorbers in active galactic nuclei (AGNs), we study the ionization-state structure of the radiation-driven fountain model in a low-mass AGN and calculate the predicted X-ray spectra utilizing the spectral synthesis code Cloudy. The spectra show many absorption and emission line features originating in the outflowing ionized gas. The O VIII 0.654 keV lines are produced mainly in the polar region much closer to the supermassive black hole than the optical narrow-line regions. The absorption measure distribution of the ionization parameter (ξ) at a low inclination spreads over 4 orders of magnitude in ξ, indicating the multiphase ionization structure of the outflow, as actually observed in many type 1 AGNs. We compare our simulated spectra with the high energy resolution spectrum of the narrow-line Seyfert 1 galaxy NGC 4051. The model reproduces slowly outflowing (a few hundred kilometers per second) warm absorbers. However, the faster components with a few thousand kilometers per second observed in NGC 4051 are not reproduced. The simulation also underproduces the intensity and width of the O VIII 0.654 keV line. These results suggest that the ionized gas launched from subparsec or smaller regions inside the torus, which is not included in the current fountain model, must be an important ingredient of the warm absorbers with a few thousand kilometers per second. The model also consistently explains the Chandra/HETG spectrum of the Seyfert 2 galaxy Circinus.

Unified Astronomy Thesaurus concepts: Active galactic nuclei (16); X-ray active galactic nuclei (2035); High energy astrophysics (739); Seyfert galaxies (1447); Astrophysical black holes (98); Supermassive black holes (1663)

1. Introduction

Outflows in various physical conditions are ubiquitously observed from an active galactic nucleus (AGN). They constitute essential elements of the AGN structure, such as jets, warm absorbers, narrow emission line regions (NLRs), and tori (e.g., Elitzur & Shlosman 2006; Netzer 2015; Wada et al. 2018b; Alonso-Herrero et al. 2021). By carrying a huge amount of mass, momentum, and energy from the nucleus, these AGN-driven outflows play key roles in determining the dynamics of accretion flow onto the supermassive black hole (SMBH) and even significantly affect its environment in the host galaxy or larger scale (e.g., Fabian 2012; Harrison 2017; Veilleux et al. 2020). Thus, revealing the physical properties and origins of the outflows is important to understanding AGN feeding/feedback mechanisms.

Outflows of mildly ionized gas can be recognized in the ultraviolet (UV) to soft X-ray ($\lesssim$2 keV) spectrum of an AGN by blueshifted absorption line and edge features (see, e.g., Kaastra et al. 2000, 2002). They are phenomenologically referred to as "warm absorbers," which are detected in the X-ray spectra of about half of the nearby type 1 AGNs (e.g., Reynolds 1997; Laha et al. 2014). With spectral fitting, one can derive the ionization parameter of the absorbers, $\xi = L_{\rm ion}/n_{\rm H}r^2$ (where $L_{\rm ion}$ is the AGN luminosity,[6] $n_{\rm H}$ is the hydrogen number density, and r is the distance from the ionizing source), the column density ($N_{\rm H}$), and the outflow velocity ($v_{\rm out}$). It is also possible to constrain $n_{\rm H}$ and/or r using other diagnostics, such as population ratios among different energy levels of the same ions (e.g., Mao et al. 2017) and time variability (e.g., Krongold et al. 2007). The typical outflow velocities of the warm absorbers are a few hundred to a few thousand kilometers per second. They show wide ranges of values in physical parameters such as ξ and $N_{\rm H}$ (e.g., Kaastra et al. 2002; Kaspi et al. 2004; Behar et al. 2017), indicating the multiphase nature of the AGN-driven outflows. Since their outflow velocities are low, the energy and momentum outflow rates carried by the warm absorbers are smaller and hence have less impact on the environments compared with ultrafast outflows (UFOs), which have velocities of $\sim$0.1c (e.g., Tombesi et al. 2010). However, due to their large mass outflow rates, the warm absorbers are important to understanding the global processes of mass flow in AGN systems, e.g., what fraction of mass fed by the host galaxy is eventually accreted by the SMBH and ejected back into the surroundings.

The physical origins of the warm absorbers still remain unclear, although several theoretical models have been proposed (e.g., Krolik & Kriss 1995; Proga et al. 2000;

[6] In this paper, we define $L_{\rm ion}$ as a luminosity integrated from 13.6 eV to 13.6 keV.

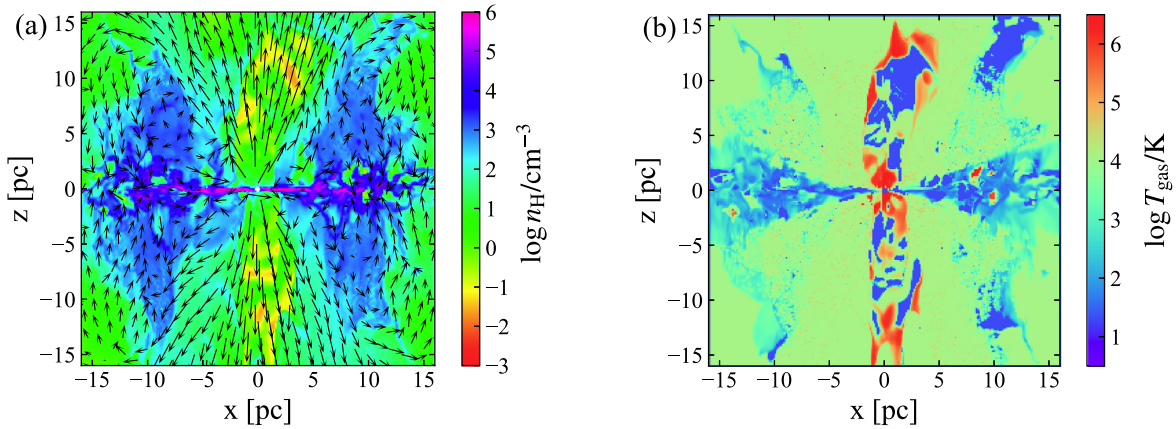

Figure 1. (a) Snapshot of hydrogen number density distribution on an x–z plane in the radiation-driven fountain model (Wada et al. 2016). The arrows represent the relative velocity fields in logarithmic scales. (b) Same as panel (a) but for temperature distribution.

Fukumura et al. 2010). Assuming that the outflow velocities of the warm absorbers correspond to the escape velocities from the gravitational potential of the SMBH, they are likely to be launched from outer accretion disks and/or torus regions. Mizumoto et al. (2019) showed that the warm absorbers can be explained as thermally driven winds from the broad-line region and torus (see, e.g., Krolik & Kriss 1995 for earlier works). However, they assumed a very simplified geometry, whereas the real structures of the interstellar medium in the central region of AGNs are still unknown. Hence, it is quite important to investigate the origins of the warm absorbers on the basis of more realistic, physically motivated dynamical models.

Wada (2012) proposed a "radiation-driven fountain" model of an AGN based on three-dimensional radiation-hydrodynamic simulations. In this model, the outflows are driven mainly by the radiation pressure to dust and the thermal energy of the gas acquired via X-ray heating, and a geometrically thick torus-like shape is naturally formed (see Figure 1). Wada et al. (2016) applied this radiation-driven fountain model to the Circinus galaxy, which is one of the closest (4.2 Mpc; Freeman et al. 1977) type 2 AGNs. The model is consistent with several observed features, such as the infrared spectral energy distribution (SED; Wada et al. 2016), the dynamics of atomic/molecular gas (Izumi et al. 2018; Wada et al. 2018a; Uzuo et al. 2021), distribution of ionized gas in the NLR (Wada et al. 2018b), and broadband X-ray spectra (Buchner et al. 2021). Mizumoto et al. (2019) also suggested that this kind of dust-driven wind may play an important role in the warm absorber acceleration.

In this paper, we present the results of mock X-ray high energy resolution spectroscopic observations based on the radiation-driven fountain in a low-mass AGN produced by Wada et al. (2016). We adopt the same approach as in Wada et al. (2018b), which calculated the intensity maps of optical emission lines (Hα, Hβ, [O III], [N II], and [S II]) utilizing the Cloudy code (Ferland et al. 2017). The three-dimensional density and velocity maps in a snapshot of the Wada et al. (2016) model are used as an input. Combining Cloudy runs along the radial direction, we make the map of the ionization state and calculate both the transmitted and scattered X-ray spectra at various inclination angles, which contain absorption and emission lines, respectively. Then, we compare these mock spectra with actual observations and investigate whether the observed spectral features of ionized absorbers (including both absorption and emission lines) can be explained by the radiation-driven fountain model.

We choose NGC 4051 (narrow-line Seyfert 1) as the comparison target. It has similar AGN parameters to those assumed in the Wada et al. (2016) model; the black hole mass, bolometric luminosity, and Eddington ratio of NGC 4051 are $(\log M_{\rm BH}/M_\odot,\ \log L_{\rm bol},\ \lambda_{\rm Edd}) = (5.6,\ 43.2,\ 0.33)$.[7] Extensive archival data of NGC 4051 observed with XMM-Newton are available. The high energy resolution spectrum observed with the Reflection Grating Spectrometer (RGS) on XMM-Newton shows a number of complex emission/absorption features indicative of multiple warm absorbers. Thus, NGC 4051 is an ideal target for our study.

The structure of this paper is as follows. Section 2 describes the overview of the radiation-driven fountain model and the numerical methods of our Cloudy simulations. The results of the simulations are summarized in Section 3. In Section 4, we compare our results with the observed X-ray spectrum of NGC 4051 and discuss the implications. The Fe Kα intensity distributions and comparison with the X-ray spectrum of the Circinus galaxy are shown in Appendix.

2. Simulations

2.1. Input Model

Here we summarize the assumptions of the radiation-driven fountain model by Wada et al. (2016), one of the dynamical models of AGN tori with supernova feedback based on three-dimensional radiation-hydrodynamic simulations. The model only considers matter distribution in the torus region ($0.125\ {\rm pc} < r < 16\ {\rm pc}$) but accounts for radiative feedback processes from the AGN, such as the radiation pressure on the surrounding material and X-ray heating. The nonspherical radiation field caused by the AGN is considered. They set the black hole mass of $M_{\rm BH}$ to $2 \times 10^6\, M_\odot$, the Eddington ratio $\lambda_{\rm Edd}$ to 0.2, the bolometric luminosity $L_{\rm bol}$ to 5×10^{43} erg s^{-1}, and the X-ray luminosity (2–10 keV) $L_{\rm X}$ to 2.8×10^{42} erg s^{-1}. The solar metallicity and cooling functions for $20\ {\rm K} \leqslant T_{\rm gas} \leqslant 10^8\ {\rm K}$ (Meijerink & Spaans 2005; Wada et al. 2009) are assumed, where $T_{\rm gas}$ is the temperature of the gas. The hydrodynamics calculations cover a $(32\ {\rm pc})^3$ region in the 256^3 grid cells. Figures 1(a) and (b) show the distributions of gas

[7] The references for the black hole mass and Eddington ratio are Koss et al. (2017) and Ogawa et al. (2021), respectively.

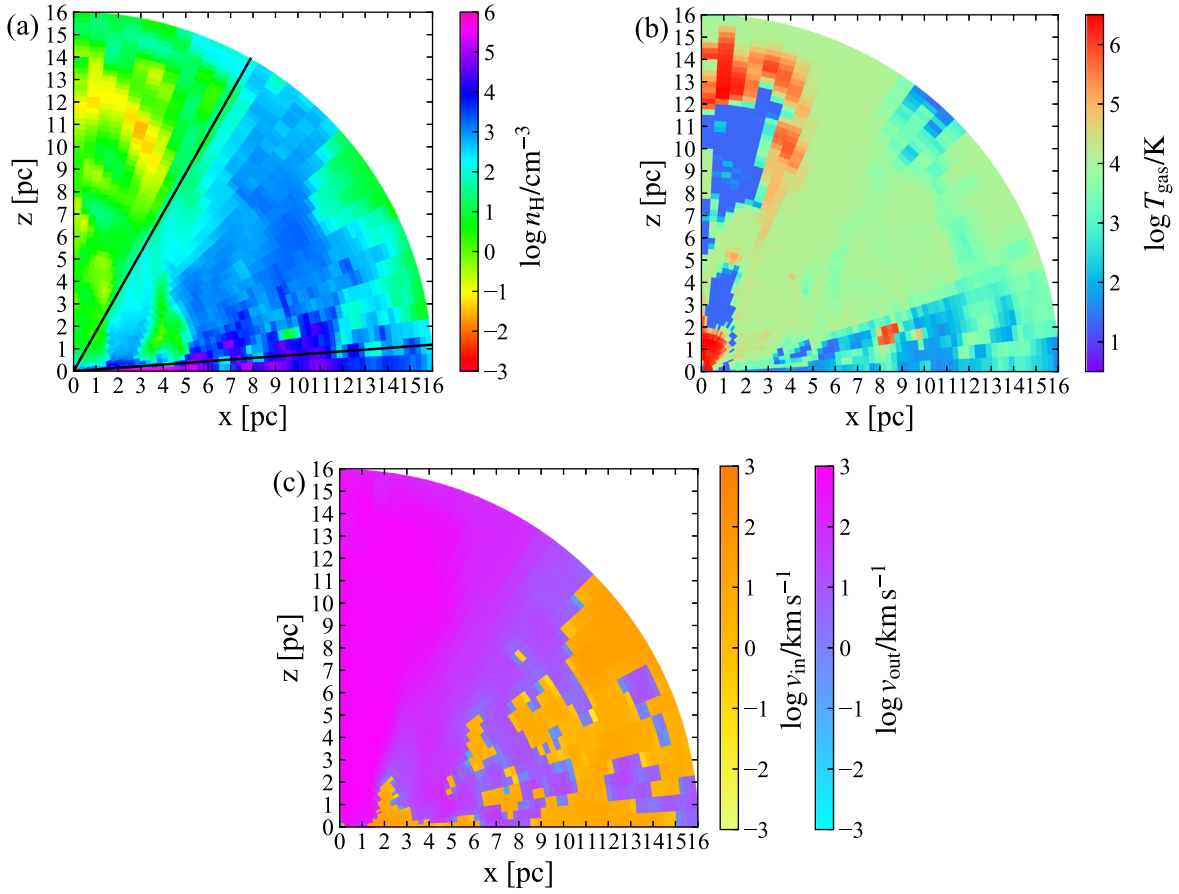

Figure 2. (a) Hydrogen number density (n_H) structure in a polar grid reformed from the original data in the radiation-driven fountain model. Black lines represents the lines of sight for $i = 30°$ and 86° from the z-axis. (b) Same as panel (a) but for the temperature (T_{gas}) structure. (c) Structure of radial inflow or outflow velocities along the lines of sight (v_{in} and v_{out}).

density and temperature, respectively. The velocity field of the gas is overplotted in Figure 1(a).

2.2. Radiative Transfer

Following the quasi-three-dimensional radiative transfer calculations in Wada et al. (2018b), we make use of Cloudy v17.02 (Ferland et al. 2017) to produce the ionization-state map and simulate the spectra. We reform the cells from the 256^3 Cartesian grid to the 64^3 uniformly spaced polar grid. Figure 2 plots the geometry of the reformed model. We input the three-dimensional maps of physical parameters (hydrogen density and temperature), obtained in a snapshot of the radiation-driven fountain model, into the Cloudy code. Figure 3 shows the input SED model at the innermost grids. It is equivalent to that obtained by Cloudy's AGN command and is represented as

$$f(\nu) = \nu^{\alpha_{UV}} \exp(-h\nu/kT_{BB}) \exp(-kT_{IR}/h\nu) \cos i + a\nu^{\alpha_X} \exp(-h\nu/E_1) \exp(-E_2/h\nu), \quad (1)$$

where $\alpha_{UV} = -0.5$, $T_{BB} = 10^5$ K, $\alpha_X = -0.7$, a is a constant that yields the X-ray–to–UV ratio $\alpha_{OX} = -1.4$, $kT_{IR} = 0.01$ Ryd, $E_1 = 300$ keV, $E_2 = 0.1$ Ryd, and i is the angle from the z-axis (i.e., inclination). The UV radiation (first term), which comes from the geometrically thin, optically thick disk, is assumed to be proportional to $\cos i$, whereas the X-ray component (second term) is assumed to be isotropic.

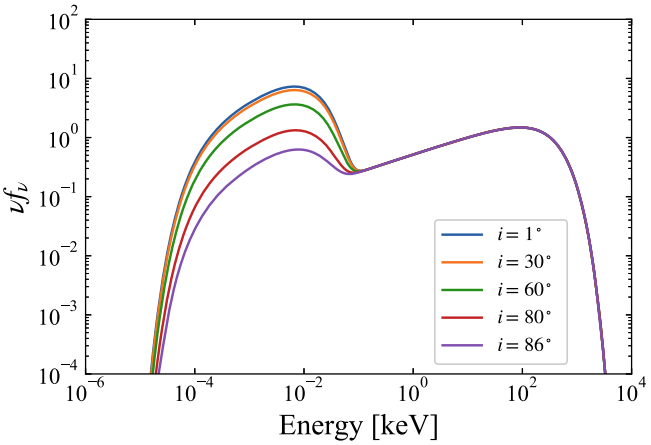

Figure 3. Incident SED models of the AGN at the innermost grids for inclination angles of $i = 1°$, 30°, 60°, 80°, and 86° (top to bottom). The vertical axis has an arbitrary unit of νf_ν, where f_ν is the energy flux at the frequency ν.

We run a sequence of Cloudy simulations along the radial direction from the central source to the outer boundary at $r = 16$ pc, where the output spectrum (net transmitted spectrum, which is the sum of the attenuated incident radiation and the diffuse emission emitted by the photoionized plasma) from a cell is used as the input spectrum to the next (outer) cell by taking into account the velocity field of each cell. Here we

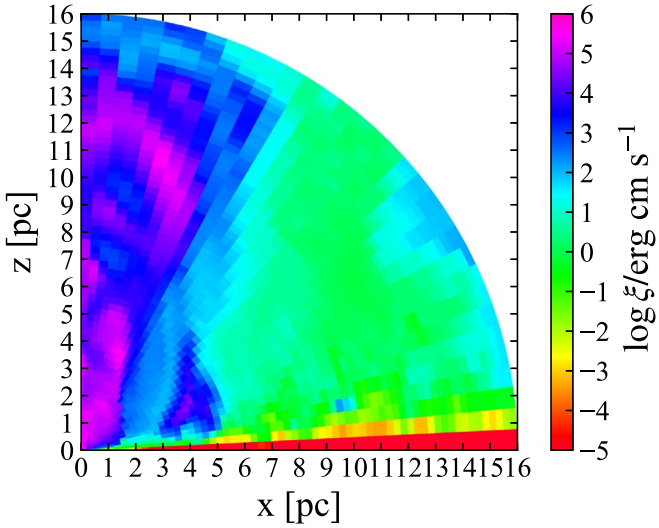

Figure 4. Structure of the ionization parameter (ξ) obtained by the Cloudy calculation.

assume that the density structure in each cell is uniform.[8] For simplicity, we also assume that the net transmitted radiation is the primary ionizing source, and the scattered radiation from the surrounding regions out of the line of sight is ignored. To confirm the validity of this assumption, we calculate the differences of the ionization parameters ξ when the scattered components from the adjacent cells out of the line of sight are added to the input spectrum in each run. To estimate the scattered components, we utilize "the reflected spectra" calculated by Cloudy, which contains Compton-scattered incident radiation and the diffuse emission. We find that the increase in the ξ parameter is $\sim$2%, on average, except for a few grid cells in the equatorial plane (>100%). Thus, we restrict the analysis for the inclination angle to $i \leqslant 88°$. After we calculate the ionization state and spectra in all cells, we integrate the reflected spectra over all cells by taking into account the optical depths in each cell along the line of sight. We refer to them as "scattered spectra" in the following.

3. Results

3.1. Ionization Structure

Figure 4 plots the map of the ionization parameter, $\xi = L_{\rm ion}/n_{\rm H}r^2$. The ionization parameter is distributed over a wide range and shows a complex structure, which mainly reflects that of hydrogen density (Figure 2(a)). It is also seen that nonisotropic radiation from the central accretion disk makes the gas in the polar region more highly ionized ($\log \xi > 3$) than that in higher-inclination regions with the same hydrogen density and distance.

Figure 5 plots the relation between the ionization parameter (ξ) and the outflow velocity ($v_{\rm out}$) for the cells along a line of sight, where each data point is color-coded by the hydrogen column density of that cell. We show the results for two inclination angles, $i = 30°$ and 86°, which are representative of type 1 and 2 AGNs, respectively (see Section 4.2 and Appendix appendix). As noticed, at the low inclination angle

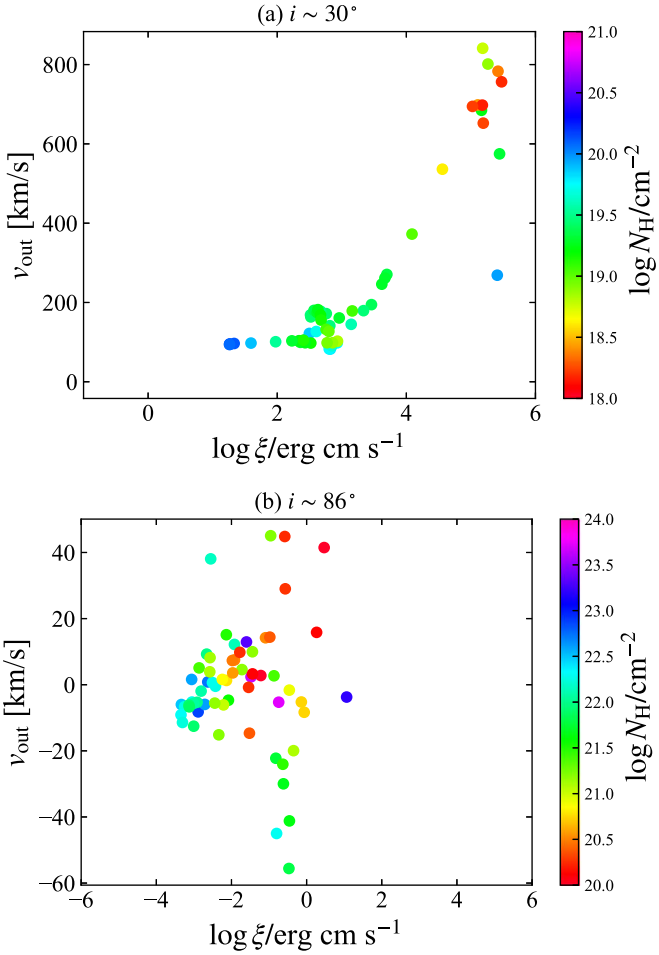

Figure 5. Relation between the ionization parameter (ξ) and outflow velocity ($v_{\rm out}$) for the grid cells along a line of sight. Each data point is color-coded by the hydrogen column density in the cell. (a) For $i = 30°$. (b) For $i = 86°$.

(Figure 5(a)), ξ is well correlated with $v_{\rm out}$, except for the highest ionization states corresponding to the closest region to the SMBH. In the polar region, the gas is almost spherically expanding; therefore, from mass conservation, we expect that $v_{\rm out} \propto 1/(n_{\rm H}r^2)$ and hence $\xi \propto v_{\rm out}$. By contrast, no clear correlation is found for the high-inclination case (Figure 5(b)). In the region closer to the equatorial plane, the gas motion is dominated by random motion caused by the backflow, turbulence, and supernova feedback, rather than the coherent motion of outflow. This makes $v_{\rm out}$ smaller (<40–60 km s^{-1}) and more complex. See, for example, Wada & Norman (2002) and Kawakatu & Wada (2008) on the effect of supernova feedback on the turbulent structures of the circumnuclear disk. Note that the radiation-driven outflows from which the warm absorbers originate are not directly affected by the supernova feedback. It is notable that the column density is large ($\log N_{\rm H} > 24$ in total) and the radial velocity is relatively slow (a few tens of kilometers per second) in this region.

3.2. X-Ray Spectra

Figures 6(a), (b), and (c) plot examples of the transmitted, scattered, and total spectra, respectively, for five inclination angles ($i = 1°$, 30°, 60°, 80°, and 86°). The spectra are characterized by many absorption line and edge features and

[8] This assumption should be verified by future numerical simulations with a higher resolution, but we confirmed that the spectral properties of the NLR, which also originated in the outflow, are reproduced with the same assumption (see Wada et al. 2018b).

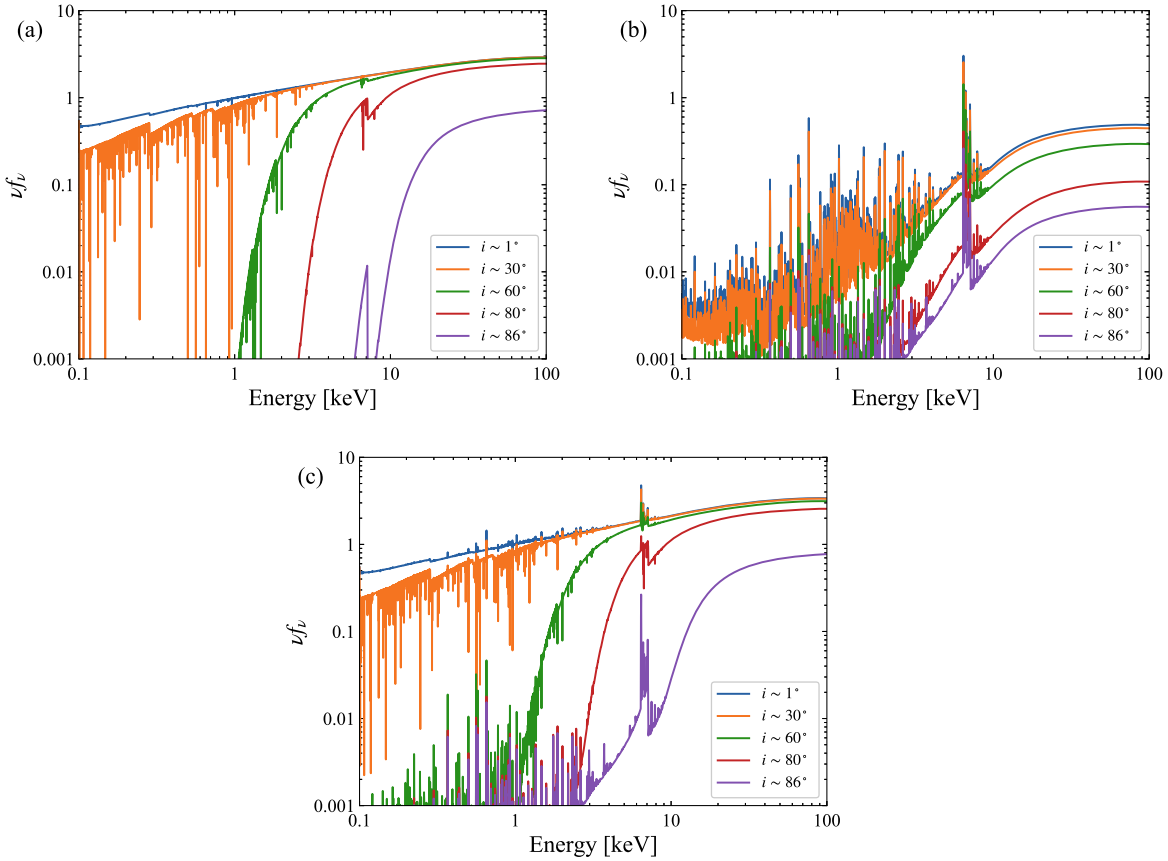

Figure 6. Simulated X-ray spectral models in units of νf_ν for inclinations of $i = 1°$, 30°, 60°, 80°, and 86° (top to bottom). (a) Transmitted spectra (attenuated incident radiation). (b) Scattered spectra, which contain Compton-scattered incident radiation and diffuse emission from all cells. (c) Total (transmitted + scattered) spectra.

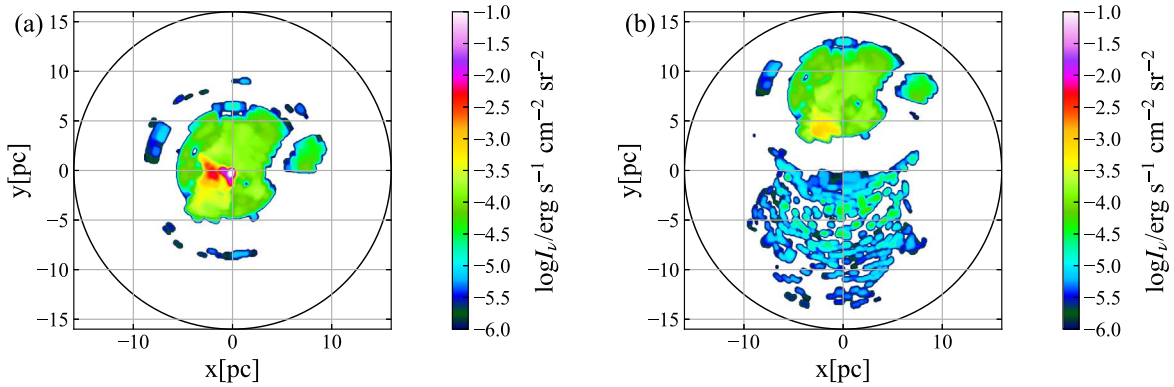

Figure 7. (a) Surface brightness distribution of O VIII Lyα at 0.654 keV for the inclination angle $i = 0°$. (b) Same as panel (a) but for $i = 30°$.

emission lines. The transmitted spectra are absorbed by materials in the line of sight and show many absorption lines by ionized gas in the 0.1–2 keV bandpass at low-to-medium-inclination angles, whereas the absorption features are very weak at $i = 1°$ because of the low line-of-sight hydrogen column density. These results indicate that, even if the presence of warm absorbers is universal in AGNs, they can be directly observed only in a certain range of inclination angles. Ionized emission lines such as hydrogen and helium-like oxygen lines at ∼0.654 and 0.56 keV, respectively, are seen in the scattered spectra in all inclination angles. In addition to the emission lines from mildly to highly ionized gas (e.g., O VIII Lyα and O VII Heα lines), iron Kα fluorescence lines at ∼6.4 keV from cold matter are also produced.

3.3. O VIII Lyα Intensity Distribution

The Cloudy simulations enable us to investigate the spatial distribution of line intensity emitted by the irradiated gas. To make a surface brightness map that could be compared with a virtual high spatial resolution observation, we integrate the line intensity along the lines of sight, taking into account absorption in each cell according to the optical depth. Figures 7(a) and (b) plot the surface brightness maps at 0.654 keV (corresponding to Lyα of O VIII) viewed from $i = 0°$ and 30°, respectively. As noticeable from the map at $i = 30°$, the lines produced on the upper side of the outflow are dominant in the observed spectrum because those on the bottom side are largely absorbed by the intervening gas. The gap at $y = 0$–5 pc is due to the absorption by the optically thick inner torus region. The O VIII

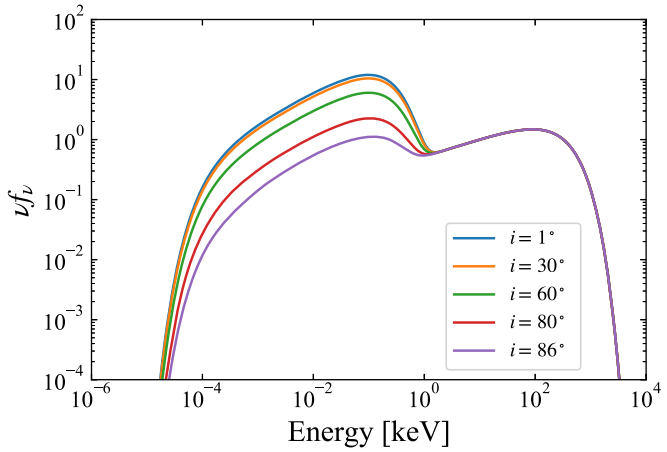

Figure 8. Incident SED models of NGC 4051 at the innermost grids for inclination angle of $i = 1°$, 30°, 60°, 80°, and 86° (top to bottom). The vertical axis has an arbitrary unit of νf_ν.

distribution shows a conical shape similar to [O III] 5007 Å(Wada et al. 2018b), although the O VIII Lyα-emitting region is located closer to the SMBH than the [O III] 5007 Å.

4. Comparison with Observations

In this section, we compare the results of our mock observations of a radiation-driven fountain with actual observations regarding the properties of the ionized absorbers and X-ray spectra. For the comparison object with a low inclination, where the warm absorbers are directly observed, we have selected NGC 4051. For a high-inclination case, we show the comparison with the Circinus galaxy (Seyfert 2) in Appendix A.2. Wada et al. (2016) adopted the same AGN parameters as those of the Circinus galaxy, $(\log M_{\rm BH}/M_\odot, \log L_{\rm bol}, \lambda_{\rm Edd}) = (6.3, 43.7, 0.2)$.

In order to make a precise comparison with NGC 4051, we performed the Cloudy simulations by changing the input SED to that more suitable for NGC 4051. This is mainly because NGC 4051 shows a strong soft excess component in the 0.4–1 keV band over the power-law component (e.g., Nucita et al. 2010; Mizumoto & Ebisawa 2017; Ogawa et al. 2021). To find an appropriate SED model of NGC 4051, we performed an SED fitting with Equation (1) using the time-averaged data of the XMM-Newton (Jansen et al. 2001) EPIC/pn and optical monitor (OM). We derived $T_{\rm BB} = 2 \times 10^6$ K, $\alpha_{\rm X} = -0.7$, and $\alpha_{\rm OX} = -1.3$. The other parameters are fixed at the values adopted in the previous simulations. Since $T_{\rm BB}$ is 20 times larger than that in Wada et al. (2018b), the prominent soft excess component appears in the 0.4–1 keV band. The ionizing luminosity $L_{\rm ion}$ (0.0136–13.6 keV) and the ionization parameters ξ are increased by a factor of ∼5 (i.e., $\log \xi$ is increased by ∼0.7) compared with the original SED. We assumed that the contamination from the host galaxy has negligible effects on the OM data. Figure 8 shows input SED models at five inclination angles ($i = 1°$, 30°, 60°, 80°, and 86°). The output spectra of the transmitted, scattered, and total components are plotted in Figure 9.

Note that the SEDs assumed in the Cloudy simulation for NGC 4051 are not strictly the same as those assumed for the Circinus galaxy by Wada et al. 2016 (see Figures 3 and 8). However, as Wada (2015) showed, the structure of the radiation-driven fountain will not change significantly as long as the Eddington ratio is similar (in the range of 0.2–0.3). Therefore, we here try to compare the fountain model and the X-ray warm absorbers in NGC 4051.

4.1. Ionized Absorbers

We investigate the absorption measure distribution (AMD) of ξ and $v_{\rm out}$, which provides quantitative information on the ionization and velocity structures of an outflow. Several attempts have been made to derive the AMDs utilizing high-resolution X-ray spectra of type 1 AGNs. In most cases, the AMDs have been found to be multipeaked, indicating the presence of multiphase ionized absorbers along the line of sight (e.g., Holczer et al. 2007; Adhikari et al. 2019). We adopt the definition by Holczer et al. (2007) for the AMD as a function of the parameter x:

$$\mathrm{AMD}(x) \equiv \frac{dN_{\rm H}}{d(\log x)}. \quad (2)$$

Figure 10 displays the AMDs of the ionization parameter ξ and outflow velocity $v_{\rm out}$ obtained at $i = 30°$ from our simulation data. As noticed, they spread over wide ranges of the parameters. In NGC 4051, ionization parameters and outflow velocities of multiple warm absorbers are consistent with our AMDs ($\log \xi = 1.4$–5 and $\log v_{\rm out} = 2.3$–2.8 have actually been observed; Krongold et al. 2007; Steenbrugge et al. 2009; Lobban et al. 2011; Pounds & Vaughan 2011; King et al. 2012; Silva et al. 2016; Mizumoto & Ebisawa 2017). These slow ionized absorbers whose $v_{\rm out}$ are a few hundred kilometers per second may be interpreted as the origin of the warm absorber outflow from the torus scale (Blustin et al. 2005).

Here we make a detailed comparison with the results of Lobban et al. (2011), who reported that four distinct ionization zones with outflow velocities of $<1000\,{\rm km\,s^{-1}}$ were required to reproduce the Chandra High-Energy Transmission Grating (HETG) data of NGC 4051 observed in 2008 November. Our AMD gives a reasonably good description of their zones 3a, 3b, and 4, whose warm absorber parameters are $(\log N_{\rm H}, \log \xi, \log v_{\rm out}) = (21.0, 2.16, 2.74)$, (20.7, 1.96, 2.91), and (21.4, 2.97, 2.85), respectively. On the other hand, zones 1 and 2, which have $(\log N_{\rm H}, \log \xi, \log v_{\rm out}) = (20.5, -0.86, 2.25)$ and (20.2, 0.60, 2.34), respectively, are not reproduced in our model; their ionization parameters are much lower than those in our model. To reproduce these low-ionization, low column density materials, numerical simulations with higher spatial resolution may be needed. Assuming $L_{\rm ion} = 10^{43}\,{\rm erg\,s^{-1}}$, $\xi = L_{\rm ion}/n_{\rm H} r^2 = 1$, and $r = 10\,{\rm pc}$, where $\log v_{\rm out}$ is ∼2 (Figure 2(c)), $n_{\rm H} \sim 10^4\,{\rm cm^{-3}}$, and therefore $N_{\rm H} = n_{\rm H}\Delta r \sim 10^{22}\,{\rm cm^{-2}}$ for $\Delta r = 0.25\,{\rm pc}$, which is the resolution along the radial direction in this work.[9] To reproduce the observed low column densities of zones 1 and 2, clumpy gas whose size is 1.5–2 orders of magnitude smaller than the current resolution must be considered.

In addition to these relatively slow components, faster ones with $v_{\rm out} > 4000\,{\rm km\,s^{-1}}$ are also detected (Steenbrugge et al. 2009; Lobban et al. 2011; Pounds & Vaughan 2011; Silva et al. 2016; Mizumoto & Ebisawa 2017). The latter cannot be reproduced by our current model. This is because the model does not include any matter inside the innermost numerical grid (i.e., $r = 0.125\,{\rm pc}$), where the escape velocities for a black hole mass of $2 \times 10^6 M_\odot$ are $>370\,{\rm km\,s^{-1}}$. Assuming that the

[9] The spatial resolution of the original hydrodynamic grid data is 0.125 pc (Wada et al. 2016).

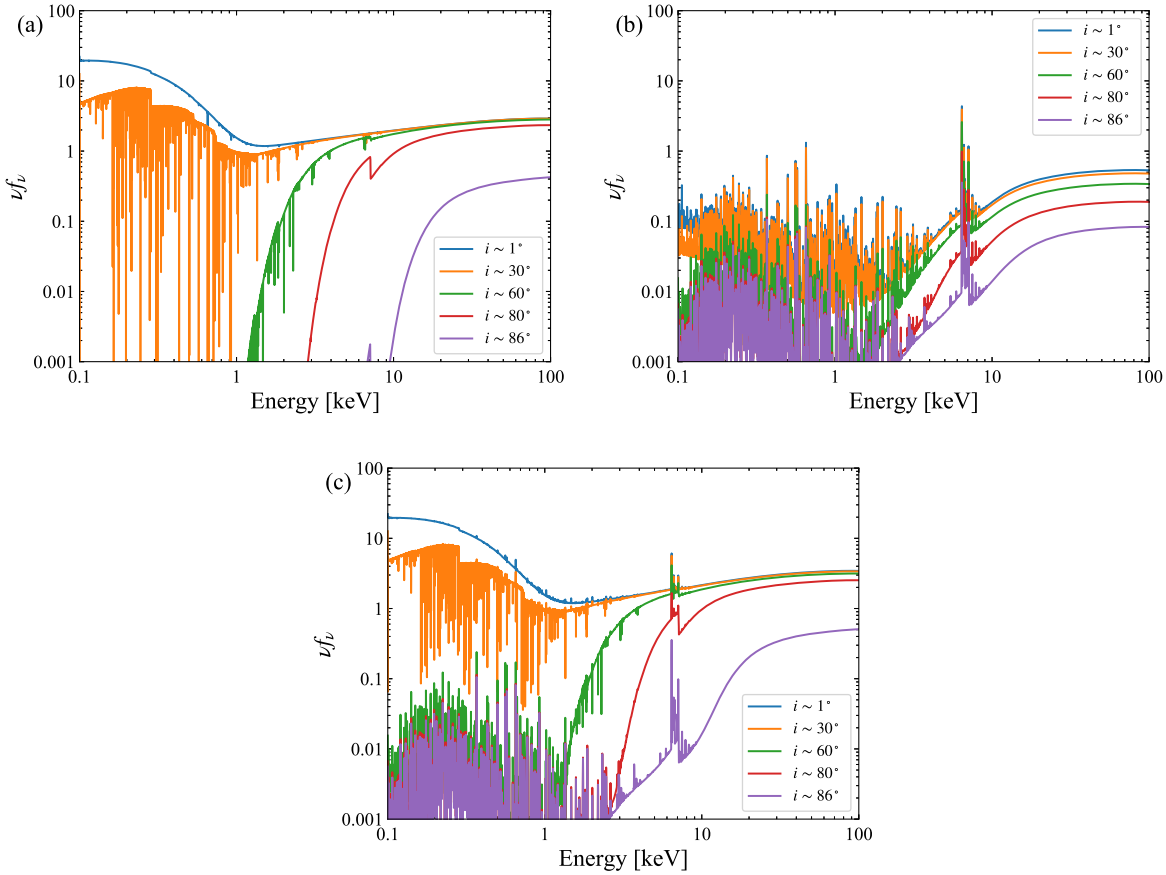

Figure 9. Simulated X-ray spectral models for NGC 4051 in units of νf_ν for inclinations of $i = 1°$, 30°, 60°, 80°, and 86° (top to bottom). (a) Transmitted spectra (attenuated incident radiation). (b) Scattered spectra, which contain Compton-scattered incident radiation and diffuse emission from all cells. (c) Total (transmitted + scattered) spectra.

outflow velocity corresponds to the escape velocity, these faster outflows should be launched at regions closer to the SMBH than the torus, such as the line-driven wind (e.g., Nomura & Ohsuga 2017; Nomura et al. 2020, for UFOs). In fact, recent radiation-hydrodynamic simulations suggest that, if the dusty gas of a thin disk continues to the inner 0.01 pc under the nonspherical UV radiation field,[10] the gas can be blown away with outflow velocities of $>1000\,\mathrm{km\,s^{-1}}$ (Y. Kudoh et al., in preparation). This fast outflow may be able to explain the properties of the observed fast warm absorbers. Another possibility is the magnetically driven outflows (e.g., Fukumura et al. 2010, 2014), but simulations of magnetic winds depend on the (currently unknown) magnetic field configuration.

4.2. X-Ray Spectrum

We compare our simulated spectra with the high energy resolution spectrum of NGC 4051 observed with XMM-Newton/RGS (den Herder et al. 2001). Our purpose is to check to what extent our simulations may produce the observed spectrum in order to obtain insights on the AGN structure. Efforts to find spectral models that are fully consistent with the observed spectrum are beyond the scope of this paper.

We analyzed the archival data observed in 2009 May–June (ObsIDs 0606320101, 0606320201, 0606320301, 0606320401, 0606321301, 0606321401, 0606321501, 0606321601, 0606321701, 0606321801, 0606321901, 0606322001, 0606322101, 0606322201, and 0606322301) using Science Analysis Software (SAS) version 17.0.0 and calibration files released on 2018 June 22. These observation epochs are different from that of the Chandra/HETG observation discussed in the previous subsection (Lobban et al. 2011). The RGS data were reprocessed with RGSPROC. We stacked all of the data to create the highest signal-to-noise ratio time-averaged spectrum.

We fit the spectrum in the 0.4–1.6 keV range with a model based on our simulations using the Cash statistic (Cash 1979). In the Xspec terminology, the model is represented as "phabs×(mtable{fountain_T.fits}×zcutoffpl1 + zcutoffpl2 + atable{fountain_S.fits})". The phabs term represents the Galactic absorption fixed at $N_\mathrm{H} = 1.20 \times 10^{20}$ cm^{-2} (the total Galactic H I and H_2 value given by Willingale et al. 2013). We use zcutoffpl1 and zcutoffpl2 to represent the first and second terms in Equation (1), respectively. The table model atable{fountain_S.fits} represents the scattered spectra of our simulation, whereas mtable{fountain_T.fits} takes into account the absorption to the transmitted component. The free parameters are the cutoff energy and normalization of zcutoffpl1, the normalization of zcutoffpl2, and the inclination and azimuthal angles in the two table models. The normalization of atable{fountain_S.fits} is linked to that of zcutoffpl2, the photon index of zcutoffpl1 is fixed at 1.5, and the

[10] The dust sublimation radius r_sub assuming spherical radiation is given by the formula of Barvainis (1987), $r_\mathrm{sub} = 1.3(L_\mathrm{UV}/10^{46}\ \mathrm{erg\ s^{-1}})^{0.5}(T_\mathrm{sub}/1500\ \mathrm{K})^{-2.8}$ pc, where L_UV is the UV luminosity and T_sub is the dust sublimation temperature. Adopting $L_\mathrm{UV} = 2 \times 10^{43}$ erg s^{-1} and $T_\mathrm{sub} = 1500$ K, we obtain $r_\mathrm{sub} = 0.05$ pc for NGC 4051. However, if anisotropic radiation from the accretion disk is taken into account, r_sub can be smaller than this value at the surface of a thin disk (see, e.g., Kawaguchi & Mori 2010).

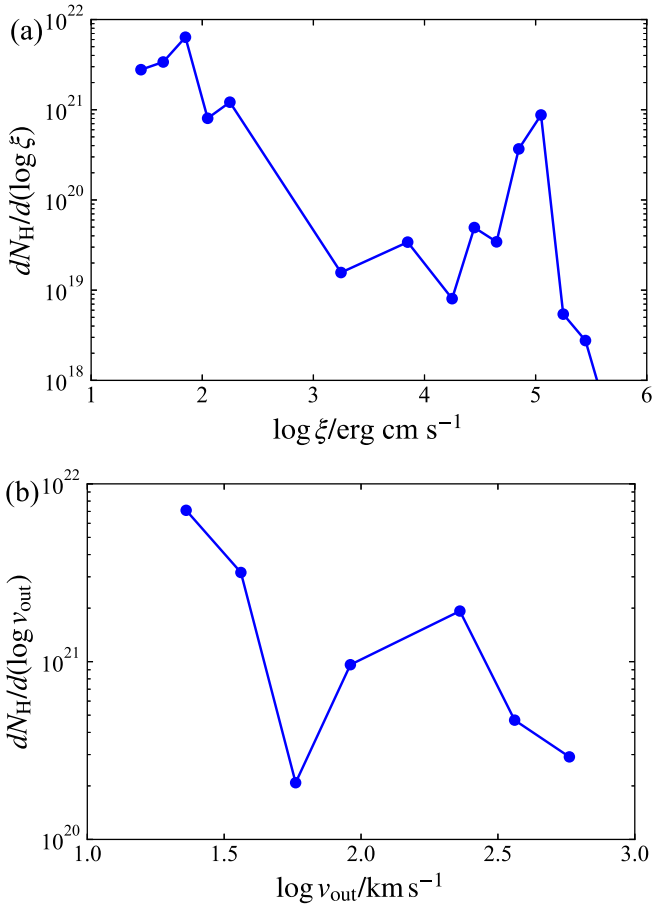

Figure 10. Model-predicted AMDs for $i = 30°$, which corresponds to the best-fit inclination angle of NGC 4051. (a) That of $\log\xi$. (b) That of $\log v_{out}$.

photon index and cutoff energy of zcutoffpl2 are fixed at 1.7 and 300 keV, respectively.

Figure 11(a) plots the observed spectrum of NGC 4051 and the best-fit model folded with the energy responses (corrected for the effective area). We obtain the best-fit inclination angle of $\approx 30°$ ($C/\mathrm{dof} = 9621/2304$). It is seen that our model reproduces many weak absorption features, particularly at energies below 0.6 keV. As mentioned above, however, it cannot reproduce the strong absorption features at $\geqslant$0.9 keV, which are produced by fast warm absorbers with $v_{out} \sim 4000$–6000 km s^{-1} (Pounds & Vaughan 2011; Silva et al. 2016; Mizumoto & Ebisawa 2017). If a fast component with $\log\xi \sim 2.6$, $\log N_H \sim 22.2$, and $v_{out} \sim 4700$ km s^{-1} is added to our model, these absorption features can be reproduced (Figure 11(b)), and the fit is much improved ($C/\mathrm{dof} = 7944/2301$).

It is also noteworthy that the simulated spectra have weaker emission lines than the observed data; the equivalent width of O VIII Lyα is a factor of $\sim$8 smaller than that of the observed result (Mizumoto & Ebisawa 2017). These emission lines may also come from regions inside the space where the hydrodynamic simulations were performed (i.e., <0.125 pc). In fact, the line width of O VIII Lyα, $\sigma = 0.1$ Å (or 1600 km s^{-1}; Mizumoto & Ebisawa 2017), is too broad to be produced by our model. Fast warm absorbers launched at $r < 0.125$ pc (see Section 4.1) might produce these emission lines.

Our model also shows some discrepancies with the observed spectrum in the Fe M-shell unresolved transition array (UTA) feature around 0.7 keV. This is mainly because the column density and outflow velocity of the best-fit model do not correctly represent those in the actual data. It is also noticeable that the model overestimates the flux around 0.5–0.53 keV. We infer that this is because the model does not well reproduce the K-edge feature from H-like carbon ions at 0.49 keV (Kramida et al. 2020). At the best-fit inclination angle, which is mainly determined by the UTA feature, carbon atoms are almost fully ionized, and hence the edge structure is very weak. Here one should also note that the three-dimensional substructures of the absorbers could be highly time-variable. In fact, as Schartmann et al. (2014) showed (see their Figure 6), the observed SEDs, especially in the short wavelengths, vary by more than 2 orders of magnitude due to the absorption for a given inclination angle over 0.1–1 Myr.

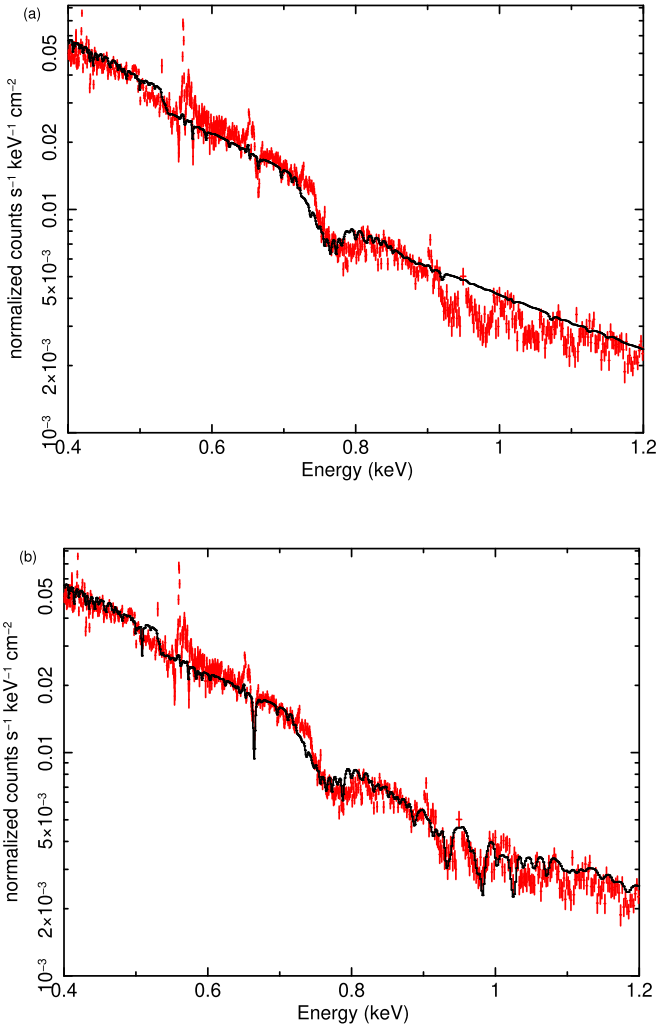

Figure 11. (a) Spectrum of NGC 4051 observed with XMM-Newton/RGS (red). It is folded with the energy responses but corrected for effective area. The solid curve represents the best-fit model based on our Cloudy simulations. (b) Same as panel (a) but fit with the model including a fast warm absorber component.

5. Conclusions

1. We have investigated the ionization state and X-ray spectra of the radiation-driven fountain model around a low-mass AGN (Wada et al. 2016) utilizing the Cloudy code.
2. The model predicts multiphase ionization structure around the SMBH, which is actually observed in ionized

outflows of AGNs. The simulated spectra show many absorption features and emission lines of ionized materials, which depend highly on inclination angle.

3. We compare our mock observations with the actual spectrum of NGC 4051. Although the radiation-driven fountain model accounts for warm absorbers with low ionization parameters ($\log \xi \lesssim 2$) and low outflow velocities of >a few hundred kilometers per second, it cannot reproduce faster ones with a few thousand kilometers per second. Also, our simulated spectra show a weaker and narrower O VIII Lyα emission line than the observed one by factors of $\sim$8 and $\sim$2, respectively.
4. These results suggest that additional components originating from the region closer to the SMBH than the torus via, e.g., line-driven winds produced in the accretion disk must be an important ingredient of the warm absorbers in AGNs.

This work was supported by JSPS KAKENHI Grant Numbers JP21J13894 (S.O.), JP20H01946 (Y.U.), JP21H04496 (K.W. and Y.U.), and JP21K13958 (M.M.). We are grateful to R. Uematsu for kindly providing us with the spectra of the Circinus galaxy, which he had analyzed. M.M. acknowledges the Hakubi project at Kyoto University. This research has made use of Cloudy. This research has also made use of data obtained with XMM-Newton, an ESA science mission with instruments and contributions directly funded by ESA Member States and NASA, and data and software provided by the High Energy Astrophysics Science Archive Research Center (HEASARC) and the Chandra X-ray Center (CXC). The radiation-hydrodynamic simulations were performed on a Cray XC50 supercomputer at the Center for Computational Astrophysics, National Astronomical Observatory of Japan.

Facilities: XMM-Newton, Chandra.

Software: HEAsoft (v6.26.1; NASA High Energy Astrophysics Science Archive Research Center (HEASARC) 2014), SAS (v17.0.0; Gabriel et al. 2004), XSPEC (v12.10.1f; Arnaud 1996), Cloudy (v17.02; Ferland et al. 2017).

Appendix A
Cold Reflectors in the Radiation-driven Fountain Model

For reference, we also investigate the nature of cold reflectors in the radiation-driven fountain model, with a particular focus on the fluorescence Fe Kα line.

A.1. Fe Kα Intensity Distribution

Figure A1 plots the surface brightness maps of lowly ionized Fe Kα lines at 6.4 keV. When viewed from nearly edge-on, the Fe Kα lines mainly come from the far side of the inner torus. This is consistent with the results of a clumpy torus model (XCLUMPY; Tanimoto et al. 2019) studied by Uematsu et al. (2021), who investigated the locations of Fe Kα emitting regions with Monte Carlo ray-tracing simulations.

A.2. X-Ray Spectrum: Comparison with Circinus Galaxy

We also compare our simulated spectra with the observed data of the Circinus galaxy, to which the AGN parameters in Wada et al. (2016) are tuned (Section 2.1). We utilize the HETG (Canizares et al. 2005) on the Chandra (Weisskopf et al. 2002) spectrum as used in Uematsu et al. (2021). They analyzed the data from all 13 observations (ObsIDs 374, 62877, 4770, 4771, 10226, 10223, 10832, 10833, 10224, 10844, 10225, 10842, and 10843) and created the time-averaged spectrum for a total exposure of 0.62 Ms. We adopt the model in the Xspec terminology "phabs$\times$(zcutoffpl + atable{fountain_S.fits} + zgauss)". The phabs and atable {fountain_S.fits} terms are the same as those of the model for NGC 4051. The zcutoffpl term also corresponds to the zcutoffpl2 term of the model for NGC 4051. The Galactic absorption is fixed at $N_{\rm H} = 7.02 \times 10^{21}$ cm^{-2}. We add zgauss as the Compton shoulder component of the Fe Kα line at 6.4 keV, which cannot be reproduced in the Cloudy code, where multiple scattering processes are ignored.

The observed spectrum and the best-fit model folded with the energy responses of the Circinus galaxy are plotted in Figure A2. We obtain a best-fit inclination angle of $\sim$87°, which is consistent with the previous studies, in which the infrared SED, molecular lines in radio, and X-ray continuum spectra are compared with observed ones (Wada et al. 2016; Izumi et al. 2018; Buchner et al. 2021; Uzuo et al. 2021). Our model gives a reasonably good description of the observed spectrum except for the intensities of the emission lines. This indicates that additional contributions are needed, as in the case of NGC 4051. One candidate would be the disk located inside the torus region and/or outflows launched from it. This may be in line with the argument by Buchner et al. (2021) that additional matter inside $r \sim 0.1$ pc is necessary to account for the shape of the broadband X-ray spectrum of the Circinus galaxy.

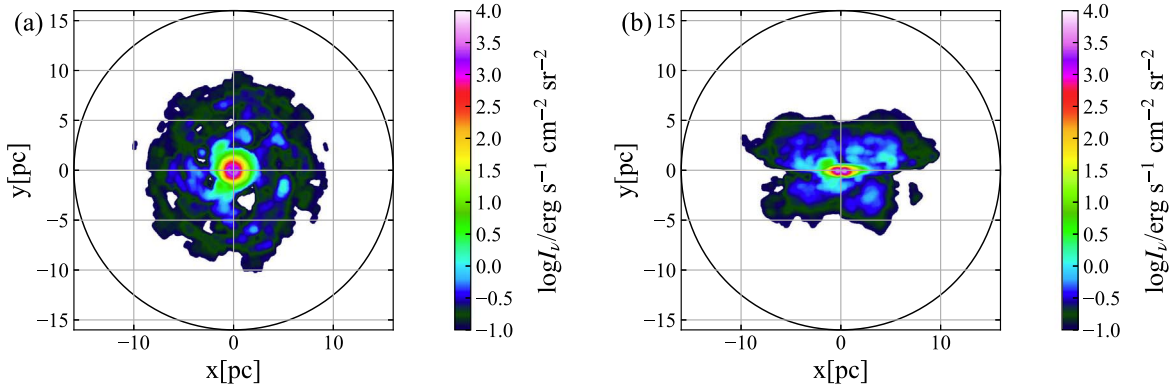

Figure A1. (a) Surface brightness distribution of Fe Kα at 6.4 keV for $i = 0°$. (b) Same as panel (a) but for $i = 80°$.

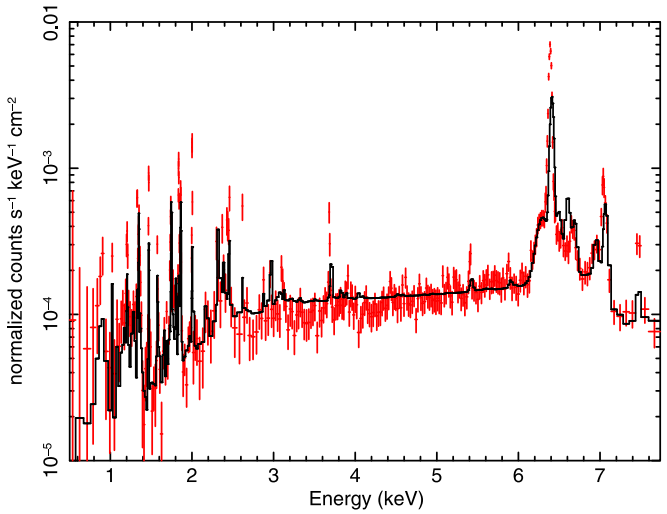

Figure A2. Spectrum of the Circinus galaxy observed with Chandra/HETG (red; MEG below 2 keV, HEG above 2 keV). It is folded with the energy responses but corrected for effective area. The solid curve represents the best-fit model based on our Cloudy simulations.

ORCID iDs

Shoji Ogawa https://orcid.org/0000-0002-5701-0811
Yoshihiro Ueda https://orcid.org/0000-0001-7821-6715
Keiichi Wada https://orcid.org/0000-0002-8779-8486
Misaki Mizumoto https://orcid.org/0000-0003-2161-0361

References

Adhikari, T. P., Różańska, A., Hryniewicz, K., Czerny, B., & Behar, E. 2019, ApJ, 881, 78
Alonso-Herrero, A., García-Burillo, S., Hoenig, S. F., et al. 2021, A&A, 652, A99
Arnaud, K. A. 1996, in ASP Conf. Ser. 101, Astronomical Data Analysis Software and Systems V, ed. G. H. Jacoby & J. Barnes (San Francisco, CA: ASP), 17
Barvainis, R. 1987, ApJ, 320, 537
Behar, E., Peretz, U., Kriss, G. A., et al. 2017, A&A, 601, A17
Blustin, A. J., Page, M. J., Fuerst, S. V., Branduardi-Raymont, G., & Ashton, C. E. 2005, A&A, 431, 111
Buchner, J., Brightman, M., Baloković, M., et al. 2021, A&A, 651, A58
Canizares, C. R., Davis, J. E., Dewey, D., et al. 2005, PASP, 117, 1144
Cash, W. 1979, ApJ, 228, 939
den Herder, J. W., Brinkman, A. C., Kahn, S. M., et al. 2001, A&A, 365, L7
Elitzur, M., & Shlosman, I. 2006, ApJL, 648, L101
Fabian, A. C. 2012, ARA&A, 50, 455
Ferland, G. J., Chatzikos, M., Guzmán, F., et al. 2017, RMxAA, 53, 385
Freeman, K. C., Karlsson, B., Lynga, G., et al. 1977, A&A, 55, 445
Fukumura, K., Kazanas, D., Contopoulos, I., & Behar, E. 2010, ApJ, 715, 636
Fukumura, K., Tombesi, F., Kazanas, D., et al. 2014, ApJ, 780, 120
Gabriel, C., Denby, M., Fyfe, D. J., et al. 2004, in ASP Conf. Ser. 314, Astronomical Data Analysis Software and Systems (ADASS) XIII, ed. F. Ochsenbein, M. G. Allen, & D. Egret (San Francisco, CA: ASP), 759
Harrison, C. M. 2017, NatAs, 1, 0165
Holczer, T., Behar, E., & Kaspi, S. 2007, ApJ, 663, 799
Izumi, T., Wada, K., Fukushige, R., Hamamura, S., & Kohno, K. 2018, ApJ, 867, 48
Jansen, F., Lumb, D., Altieri, B., et al. 2001, A&A, 365, L1
Kaastra, J. S., Mewe, R., Liedahl, D. A., Komossa, S., & Brinkman, A. C. 2000, A&A, 354, L83
Kaastra, J. S., Steenbrugge, K. C., Raassen, A. J. J., et al. 2002, A&A, 386, 427
Kaspi, S., Netzer, H., Chelouche, D., et al. 2004, ApJ, 611, 68
Kawaguchi, T., & Mori, M. 2010, ApJL, 724, L183
Kawakatu, N., & Wada, K. 2008, ApJ, 681, 73
King, A. L., Miller, J. M., & Raymond, J. 2012, ApJ, 746, 2
Koss, M., Trakhtenbrot, B., Ricci, C., et al. 2017, ApJ, 850, 74
Kramida, A., Ralchenko, Y., Reader, J. & NIST ASD Team 2020, NIST Atomic Spectra Database (ver. 5.8), National Institute of Standards and Technology, Gaithersburg, MD, https://physics.nist.gov/asd
Krolik, J. H., & Kriss, G. A. 1995, ApJ, 447, 512
Krongold, Y., Nicastro, F., Elvis, M., et al. 2007, ApJ, 659, 1022
Laha, S., Guainazzi, M., Dewangan, G. C., Chakravorty, S., & Kembhavi, A. K. 2014, MNRAS, 441, 2613
Lobban, A. P., Reeves, J. N., Miller, L., et al. 2011, MNRAS, 414, 1965
Mao, J., Kaastra, J. S., Mehdipour, M., et al. 2017, A&A, 607, A100
Meijerink, R., & Spaans, M. 2005, A&A, 436, 397
Mizumoto, M., Done, C., Tomaru, R., & Edwards, I. 2019, MNRAS, 489, 1152
Mizumoto, M., & Ebisawa, K. 2017, MNRAS, 466, 3259
Nasa High Energy Astrophysics Science Archive Research Center (Heasarc) 2014, HEAsoft: Unified Release of FTOOLS and XANADU, Astrophysics Source Code Library, ascl:1408.004
Netzer, H. 2015, ARA&A, 53, 365
Nomura, M., & Ohsuga, K. 2017, MNRAS, 465, 2873
Nomura, M., Ohsuga, K., & Done, C. 2020, MNRAS, 494, 3616
Nucita, A. A., Guainazzi, M., Longinotti, A. L., et al. 2010, A&A, 515, A47
Ogawa, S., Ueda, Y., Tanimoto, A., & Yamada, S. 2021, ApJ, 906, 84
Pounds, K. A., & Vaughan, S. 2011, MNRAS, 413, 1251
Proga, D., Stone, J. M., & Kallman, T. R. 2000, ApJ, 543, 686
Reynolds, C. S. 1997, MNRAS, 286, 513
Schartmann, M., Wada, K., Prieto, M. A., Burkert, A., & Tristram, K. R. W. 2014, MNRAS, 445, 3878
Silva, C. V., Uttley, P., & Costantini, E. 2016, A&A, 596, A79
Steenbrugge, K. C., Fenovčík, M., Kaastra, J. S., Costantini, E., & Verbunt, F. 2009, A&A, 496, 107
Tanimoto, A., Ueda, Y., Odaka, H., et al. 2019, ApJ, 877, 95
Tombesi, F., Cappi, M., Reeves, J. N., et al. 2010, A&A, 521, A57
Uematsu, R., Ueda, Y., Tanimoto, A., et al. 2021, ApJ, 913, 17
Uzuo, T., Wada, K., Izumi, T., et al. 2021, ApJ, 915, 89
Veilleux, S., Maiolino, R., Bolatto, A. D., & Aalto, S. 2020, A&ARv, 28, 2
Wada, K. 2012, ApJ, 758, 66
Wada, K. 2015, ApJ, 812, 82
Wada, K., Fukushige, R., Izumi, T., & Tomisaka, K. 2018a, ApJ, 852, 88
Wada, K., & Norman, C. A. 2002, ApJL, 566, L21
Wada, K., Papadopoulos, P. P., & Spaans, M. 2009, ApJ, 702, 63
Wada, K., Schartmann, M., & Meijerink, R. 2016, ApJL, 828, L19
Wada, K., Yonekura, K., & Nagao, T. 2018b, ApJ, 867, 49
Weisskopf, M. C., Brinkman, B., Canizares, C., et al. 2002, PASP, 114, 1
Willingale, R., Starling, R. L. C., Beardmore, A. P., Tanvir, N. R., & O'Brien, P. T. 2013, MNRAS, 431, 394